

High-performance chiral all-optical OR logic gate based on topological edge states of valley photonic crystal

Xiaorong Wang(王晓蓉), Hongming Fei(费宏明), Han Lin(林瀚), Min Wu(武敏), Lijuan Kang(康丽娟), Mingda Zhang(张明达), Xin Liu(刘欣), Yibiao Yang(杨毅彪), and Liantuan Xiao(肖连团)

Citation: Chin. Phys. B, 2023, 32 (**7**): 074205. DOI: 10.1088/1674-1056/accb41

Journal homepage: http://cpb.iphy.ac.cn; http://iopscience.iop.org/cpb

What follows is a list of articles you may be interested in

Theoretical research on the transverse spin of structured optical fields inside a waveguide

Zhiyong Wang(王智勇), Xiangru Wang(汪相如), Anran Li(李岸然), Kaiqiang Zhang(张开强), Yukun Ji(纪玉坤), and Mingyu Zhong(钟明玉)

Chin. Phys. B, 2023, 32 (**6**): 064207. DOI: 10.1088/1674-1056/acbf28

Diffraction deep neural network based orbital angular momentum mode recognition scheme in oceanic turbulence

Hai-Chao Zhan(詹海潮), Bing Chen(陈兵), Yi-Xiang Peng(彭怡翔), Le Wang(王乐), Wen-Nai Wang(王文鼐), and Sheng-Mei Zhao(赵生妹)

Chin. Phys. B, 2023, 32 (**4**): 044208. DOI: 10.1088/1674-1056/ac935e

Multi-target ranging using an optical reservoir computing approach in the laterally coupled semiconductor lasers with self-feedback

Dong-Zhou Zhong(钟东洲), Zhe Xu(徐喆), Ya-Lan Hu(胡亚兰), Ke-Ke Zhao(赵可可), Jin-Bo Zhang(张金波),Peng Hou(侯鹏), Wan-An Deng(邓万安), and Jiang-Tao Xi(习江涛)

Chin. Phys. B, 2022, 31 (**7**): 074205. DOI: 10.1088/1674-1056/ac4021

Topological phases and type-II edge state in two-leg-coupled Su-Schrieffer-Heeger chains

Tianqi Luo(罗天琦), Xin Guan(关欣), Jingtao Fan(樊景涛), Gang Chen(陈刚), and Suo-Tang Jia(贾锁堂)

Chin. Phys. B, 2022, 31 (**1**): 014208. DOI: 10.1088/1674-1056/ac3650

Symmetry-broken silicon disk array as an efficient terahertz switch working with ultra-low optical pump power

Zhanghua Han(韩张华), Hui Jiang(姜辉), Zhiyong Tan(谭智勇), Juncheng Cao(曹俊诚), Yangjian Cai(蔡阳健)

Chin. Phys. B, 2020, 29 (**8**): 084209. DOI: 10.1088/1674-1056/ab9c0b

---

High-performance chiral all-optical OR logic gate based on topological edge states of valley photonic crystal

Xiaorong Wang(王晓蓉)[1,2], Hongming Fei(费宏明)[1,2,†], Han Lin(林瀚)[3,‡], Min Wu(武敏)[1,2], Lijuan Kang(康丽娟)[1,2], Mingda Zhang(张明达)[1,2], Xin Liu(刘欣)[1,2], Yibiao Yang(杨毅彪)[1,2], and Liantuan Xiao(肖连团)[1,2]

[1] *College of Physics, Taiyuan University of Technology, Taiyuan* 030024, *China*
[2] *Key Laboratory of Advanced Transducers and Intelligent Control System, Ministry of Education, Taiyuan University of Technology, Taiyuan* 030024, *China*
[3] *School of Science, RMIT University, Melbourne, Victoria* 3000, *Australia*

(Received 26 December 2022; revised manuscript received 3 April 2023; accepted manuscript online 7 April 2023)

For all-optical communication and information processing, it is necessary to develop all-optical logic gates based on photonic structures that can directly perform logic operations. All-optical logic gates have been demonstrated based on conventional waveguides and interferometry, as well as photonic crystal structures. Nonetheless, any defects in those structures will introduce high scattering loss, which compromises the fidelity and contrast ratio of the information process. Based on the spin-valley locking effect that can achieve defect-immune unidirectional transmission of topological edge states in valley photonic crystals (VPCs), we propose a high-performance all-optical logic OR gate based on a VPC structure. By tuning the working bandwidth of the two input channels, we prevent interference between the two channels to achieve a stable and high-fidelity output. The transmittance of both channels is higher than 0.8, and a high contrast ratio of 28.8 dB is achieved. Moreover, the chirality of the logic gate originated from the spin-valley locking effect allows using different circularly polarized light as inputs, representing "1" or "0", which is highly desired in quantum computing. The device's footprint is 18 μm × 12 μm, allowing high-density on-chip integration. In addition, this design can be experimentally fabricated using current nanofabrication techniques and will have potential applications in optical communication, information processing, and quantum computing.

Keywords: topological photonics, topological edge state, valley photonic crystal, all-optical logic gate

PACS: 42.79.Ta, 42.25.Bs, 42.70.Qs, 78.67.Pt **DOI:** 10.1088/1674-1056/accb41

1. Introduction

Due to the development of augmented reality (AR)/virtual reality (VR) and big data, the increase in information traffic demands large bandwidth and reliable information processing. Optical communication and information processing have the advantages of large bandwidth, fast speed, high energy efficiency, and low heat generation. An all-optical network[1] is that the signal always exists in the form of light during the propagation and information processing, which overcomes the "electronic bottleneck" phenomenon caused by the previous optical-electrical-optical conversion.[2] It is necessary to develop an entire family of different all-optical components for all-optical networks, such as waveguides, optical switches,[3–8] wavelength division multiplexing (WDM) devices, optical delay lines, logic gates, and so forth. Currently, information processing is realized by electrical logic gates (AOLGs) based on electro-optic conversion all the time[9,10] due to the limited performance of current AOLG designs that cannot meet the requirements in applications. As a result, the speed is ultimately limited by the relatively slow electric logic gates. Therefore, designing high-performance AOLGs has become a stringent request and is key to realizing all-optical information processing.

An ideal logic gate performs operations on Boolean values, which should dissipate no power and change states instantaneously, similar to a step function. Such gates operate on discrete logic inputs and should have no propagation delay. For AOLGs, the propagation delay is neglectable due to the high speed of light. In addition, power dissipation can be minimized by achieving high transmittance. Furthermore, for photonic integrated circuit (PIC) operation, AOLGs should have a miniaturized footprint for high-density integration. In general, AOLGs that work with different spin states of photons are required for quantum computing. Therefore, AOLGs should have chiral responses to work with spin-up (right-handed circularly polarized, RCP) and spin-down (left-handed circularly polarized, LCP) photons.

Many designs of AOLGs based on different working principles have been demonstrated, such as semiconductor optical amplifier (SOA),[11–14] periodically poled lithium niobate (PPLN) waveguide,[15,16] ring resonators,[17–19] and photonic crystals (PCs).[20–22] The performance of SOA-based AOLGs is limited by spontaneous emission noise and high integration complexity. In comparison, the AOLGs based on semi-

†Corresponding author. E-mail: feihongming@tyut.edu.cn
‡Corresponding author. E-mail: han.lin2@rmit.edu.au

© 2023 Chinese Physical Society and IOP Publishing Ltd

conductor ring resonators have the advantages of simplicity and low input power. But the speed is slow. Meanwhile, the AOLGs based on PPLN waveguides have fast switching speeds and low spontaneous emission noise. However, those AOLGs strongly depend on the working temperature and the incident light's polarization states, which hinder their applications. All the AOLGs mentioned above have relatively large footprints, which makes them unsuitable for high-density on-chip integration. In comparison, the footprint of AOLGs can be significantly reduced by using nanostructures, in which PC structures[23–32] are the most widely used. Different effects and principles of PC structures have been applied to design AOLGs, such as self-collimation,[33,34] multimode interference,[35,36] interference waveguides,[37,38] and nonlinear effects.[39,40] However, all the designs above have relatively low transmittance due to the scattering loss introduced by structural defects. In addition, none of the AOLG designs, including all conventional and PC designs, can work with circularly polarized light (CPL) to maintain the spin states, which is important for quantum computing.[41–43]

The recent development of topological photonic crystals (TPCs)[44–50] allows defect-immune unidirectional transmission of topological edge states, which opens new possibilities in designing photonic devices. Among different TPC designs, valley photonic crystals (VPCs) can be achieved based on dielectric materials without an external magnetic field, thus pushing the working wavelength to the telecommunication and the visible region.[51,52] Here based on the unique spin-valley locking effect of VPCs, we design a high-performance integratable all-optical logic OR gate based on the tunable topological edge states of VPCs. We tune the working bands of the two input channels to minimize their interference, achieving stable and high-fidelity outputs. The spin-valley locking effect allows robust unidirectional transmission of CPL. The transmittance of both channels is higher than 0.8, which meets the requirements of an ideal all-optical logic gate. In addition, an ultrahigh contrast ratio of 28.8 dB is achieved. Currently, the contrast ratio of AOLGs based on conventional PC structures is mainly in the range of 10 dB–20 dB. So our design has a much higher contrast ratio than those AOLGs in recent references.[37] Furthermore, the chiral responses of the AOLGs allow using CPL with different handedness as logic inputs (logic "1" or logic "0"), which meets the requirements of quantum computing.[41–43] The footprint of the entire AOLG device is as small as 18 μm × 12 μm, allowing high-density on-chip integration. The device can be manufactured by the mature complementary metal–oxide–semiconductor (CMOS) nanofabrication technique and will find broad applications in optical information processing and quantum computing.

2. Design of the all-optical OR gate

An OR logic gate (symbolized by "‖" or "+") outputs a logic "1" if one or both the inputs are logic "1"; otherwise, it outputs a logic "0". Here, the logic "1" in an AOLG is defined as the input or the output having an incident or transmitted optical wave with a transmittance higher than 0.7. And the logic "0" is determined when the criterion is not met. According to this definition, an all-optical OR gate based on a VPC structure is designed and shown in Fig. 1(d). The gate comprises two mirror-symmetrical VPC structures, consisting of two input waveguides (INA and INB) and two output waveguides (OUT1 and OUT2). To minimize the interference between the two inputs, we tune the working bands of INA (centered at λ_1, figures 1(a) and 1(c)) and INB (centered at λ_2, figures 1(b) and 1(c)) by adjusting the radii of the lattice at the boundary (highlighted by different colors in Fig. 1(d)). Meanwhile, the working band of the output waveguide OUT1 can cover the two working bands of INA and INB. In contrast, the OUT2 is designed to have extremely low transmittance in those working bands to prevent the undesired loss through the waveguide to maximize the transmittance through OUT1. The schematics in Fig. 1 show the four possible cases of the AOLG, namely $1\|0=1$, $0\|1=1$, $1\|1=1$, and $0\|0=0$. The two numbers on the left side correspond to the inputs from INA and INB, respectively. The number on the right side shows the output of OUT1.

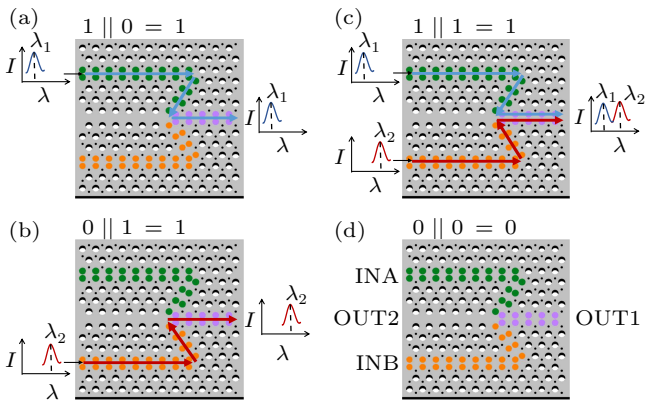


Fig. 1. The working diagrams of an all-optical OR logic gate: (a) light inputs only from INA, as $1\|0=1$; (b) light inputs only from INB, as $0\|1=1$; (c) light inputs from both INA and INB, as $1\|1=1$; (d) light inputs from neither INA nor INB, as $0\|0=0$.

The design process started with creating a honeycomb PC structure (Fig. 2(a)) composed of circular air holes embedded in a free-standing silicon substrate. The refractive index of silicon is shown in supporting information S1. The thickness of the free-standing silicon substrate (the dispersive refractive index of pure silicon is used) is $h = 220$ nm. The unit cell of this structure is composed of two sets of air holes (A and B) with the same radius ($r_A = r_B = 80$ nm), which has a C_{6V} rotational symmetry. The lattice constant is $a = 450$ nm. Here

we use commercial three-dimensional (3D) time–domain finite difference (FDTD) software (Lumerical FDTD Solutions) to calculate the photonic band structure. The band diagram of the transverse electric (TE) mode is shown in Fig. 2(c) by the dashed lines, which show a Dirac point. Then the C_{6V} symmetry is reduced to C_3 symmetry by simultaneously increasing r_A (to 120 nm) and decreasing r_B (to 40 nm) to introduce a topological photonic bandgap (1410 nm–1676 nm) due to the degeneracy of the K and K' valleys, indicated by the blue dot lines in Fig. 2(c). In this way, VPC1 is designed (left panel in Fig. 2(b)), which can be converted to VPC2 (right panel in Fig. 2(b)) by applying mirror symmetry operation. The values of the Berry curvature and topologically invariant valley Chern number C_V corresponding to the two VPCs were calculated, which are $C_V = -1$ for VPC1 and $C_V = 1$ for VPC2,[51] respectively.

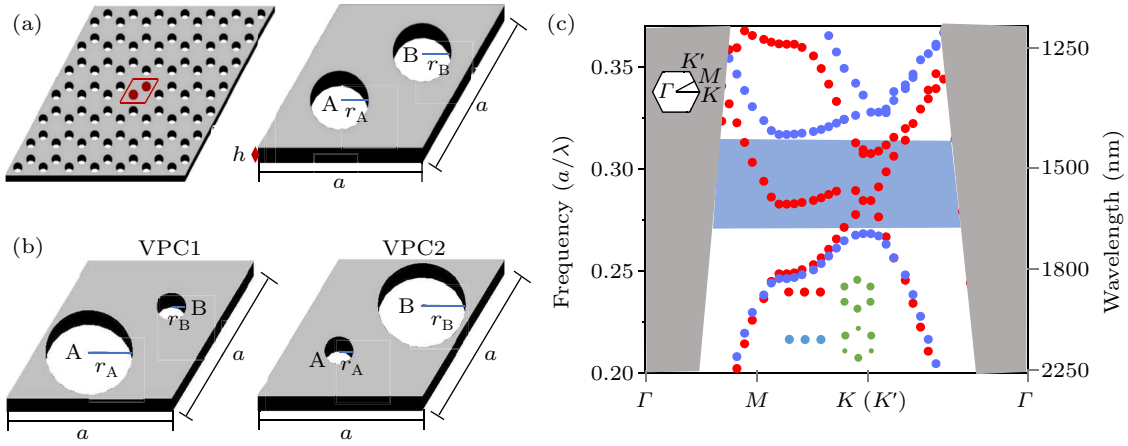


Fig. 2. Structure parameters and photonic band diagrams of PCs. (a) 3D schematics of the honeycomb PC structure; (b) 3D schematics of VPC1 and VPC2; (c) the photonic band diagram of the honeycomb PC (red dot line) and VPC1 (blue dot line), the blue shaded area marks the bandgap; the gray region marks the air cone.

3. Tuning of topological edge states

There are two possible types of boundaries, the zigzag-shape and beard-shape boundaries, which can support topological edge states. The study of the edge states of the two boundaries shows that the working bandwidth of the beard-shape boundary is narrower than the bandgap, which allows tuning the position of the working bands within the bandgap. The detail is shown in supporting information S2. In this study, we choose the beard-shape boundary as required to achieve different working bands within the bandgap. Depending on the small or large circles at the boundary, two kinds of beard-shape boundaries can be constructed: S-interface and L-interface. Due to the high transmittance of the L-interface, it is chosen for INA, INB, and OUT1. Figure 3(a) shows the schematic of a straight waveguide using the L-interface boundary. We define the radius of the large air holes at the boundary as r_e. By tuning the r_e, the working band of each waveguide can be controlled. As shown in Fig. 3(b), the decrease of r_e (120 nm, 116 nm, 110 nm) results in a redshift of the working bands due to the increased effective refractive index of the edge states.

We performed numerical simulations on 11 sets of straight waveguides using RCP incident light, with r_e gradually decreasing from 120 nm to 110 nm at a step of 1 nm. The transmittance spectra are shown in Fig. 3(c). The tuning aims to separate the working bands of INA and INB to minimize interference and achieve a stable output. According to the definition of logic "1", the working band is defined as where the forward transmittance is higher than 0.7 (TF > 0.7). The plot of the working band *versus* different radii is shown in Fig. 3(d). The working band is quite sensitive to the radius change, which presents a linear relationship with r_e (the slope is 5.792). Therefore, when r_e decreases by 1 nm, the central wavelength of the working band increases by 5.792 nm. We find three r_e values meeting our requirements, which are $r_e = 120$ nm (the working band is 1476 nm–1512 nm), $r_e = 116$ nm (the working band is 1489.7 nm–1542 nm), and $r_e = 110$ nm (the working band is 1522 nm–1582 nm), respectively. As one can see, the working bands in the cases of $r_e = 120$ nm and $r_e = 110$ nm can be well separated. Meanwhile, the working band in the case of $r_e = 116$ nm overlaps with both $r_e = 120$ nm and $r_e = 110$ nm. Therefore, we use $r_1 = 120$ nm for INA and $r_2 = 110$ nm for INB, respectively. Meanwhile, $r_3 = 116$ nm is used for OUT1. As a result, inputs from INA and INB can highly efficiently transmit through OUT1. In addition, to minimize the light leakage from OUT2, the air holes at the boundary are removed. Thus, the transmittance of OUT2 approaches zero in the range of 1450 nm–1530 nm. The detail is shown in supporting information S3.

We design Z-shape waveguides with INA or INB combined with OUT1 to study the transmission properties of different combinations. The schematics of the Z-shape waveguides are shown in Figs. 4(a) and 4(b), respectively. The green

and red circles in the Z1 and Z2 waveguides (Figs. 4(a) and 4(b)) have $r_1 = 120$ nm and $r_2 = 110$ nm, respectively. The purple circles in both waveguides have an $r_3 = 116$ nm. The transmittance spectra are plotted in Fig. 4(e). Here we choose two working wavelengths for INA and INB to achieve the function of an AOLG, which are $\lambda_1 = 1490$ nm and $\lambda_2 = 1528$ nm (marked by the dashed lines in Fig. 4(e)), respectively. Those wavelengths are chosen due to the high transmittance (TF > 0.75). The intensity distributions in the Z-shape waveguides at the two working wavelengths in Figs. 4(c) and 4(d) show that the light waves are well confined within the waveguides.

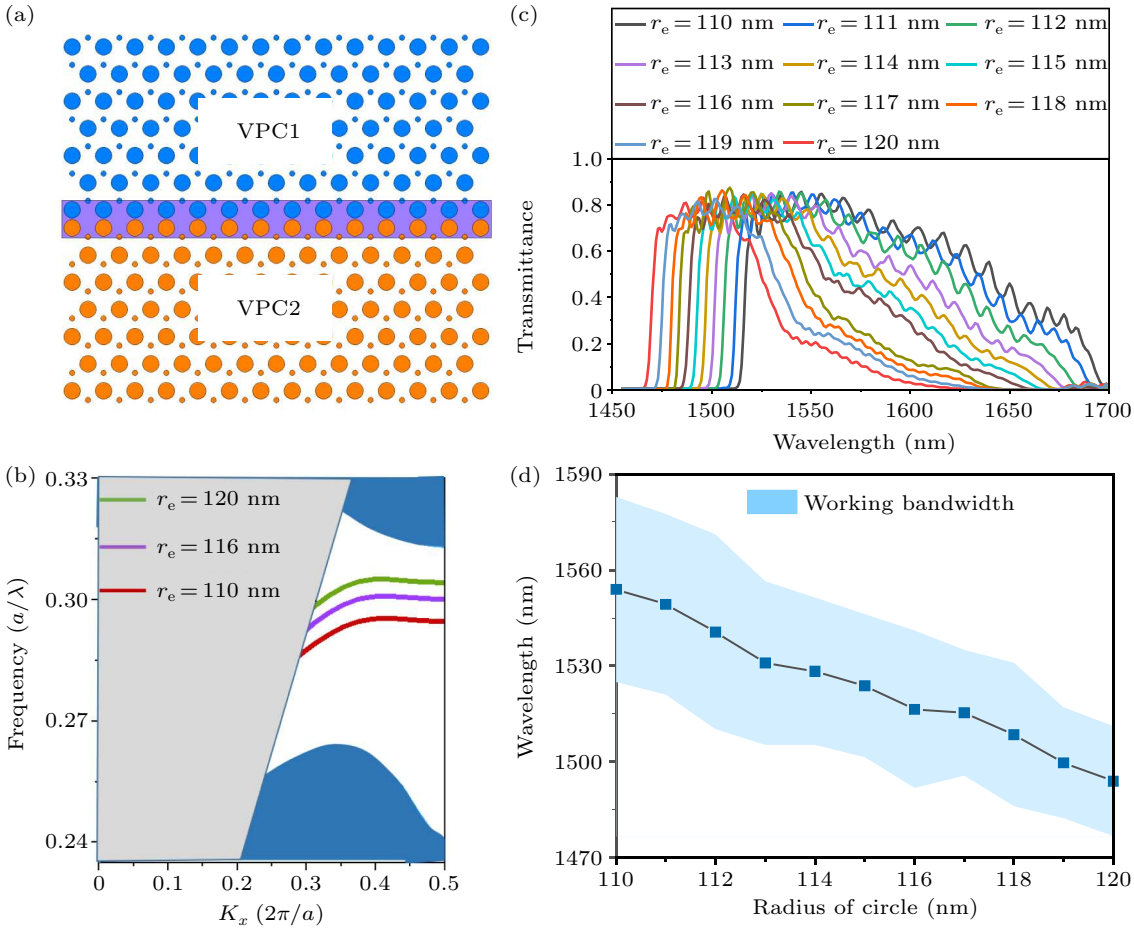


Fig. 3. (a) A schematic diagram of a straight waveguide based on the L-interface boundary (the big circles in the purple area are the air holes at the boundary, and the radius is r_e). (b) Band diagram of the valley-dependent edge states (the green, purple, and red lines correspond to $r_e = 120$ nm, $r_e = 116$ nm, and $r_e = 110$ nm, respectively). (c) Transmittance spectra of straight waveguides with different r_e. (d) The plot of working band *versus* different r_e.

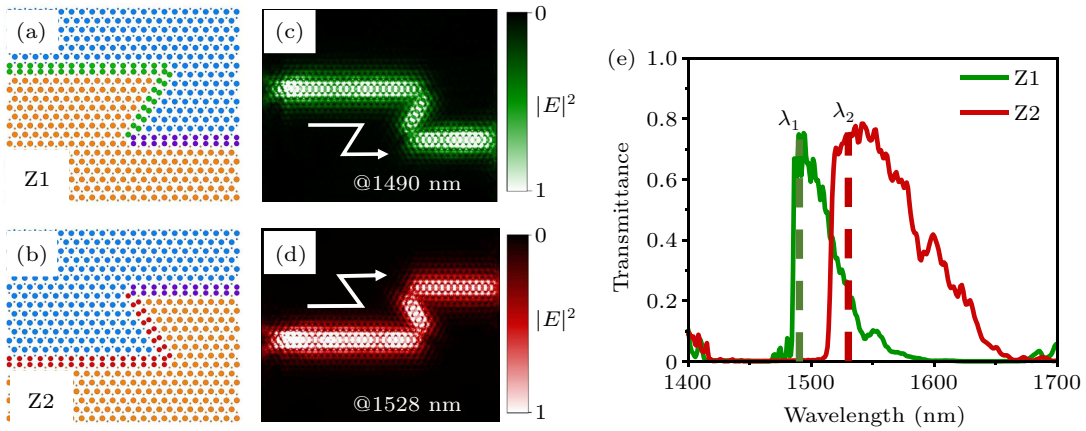


Fig. 4. Z-shape waveguide designs and transmittance. (a) Schematic diagram of Z1 waveguide composed of INA and OUT1. (b) Schematic diagram of Z2 waveguide composed of INB and OUT1. (c) The electric field intensity distributions in Z1 waveguide at $\lambda_1 = 1490$ nm. (d) The electric field intensity distributions in Z2 waveguide at $\lambda_2 = 1528$ nm. (e) Transmittance spectra of the two Z-shape waveguides.

4. Performance analysis of the designed all-optical OR gate

We then combine the two Z-shape waveguides to form the all-optical OR gate, shown in Fig. 5(a). The boundary conditions of FDTD are PML in the x–y direction and symmetric in the z direction. The input light source is RCP, a superposition of two dipole sources. The transmittance spectra of the AOLG are shown in Fig. 5(b), in which one can see different input cases from INA $(1\|0)$, INB $(0\|1)$, and INA+INB $(1\|1)$. In all three cases, the output from OUT1 has a transmittance higher than 0.7 at either $\lambda_1 = 1490$ nm or $\lambda_2 = 1528$ nm. The corresponding intensity distributions are plotted in Figs. 5(c)–5(f). When the light waves at the designed working wavelengths are input from INA (Fig. 5(c)) and INB (Fig. 5(d)) separately, they can highly efficiently transmit through the AOLG. The transmittances are 0.86 and 0.90 at the wavelengths of $\lambda_1 = 1490$ nm or $\lambda_2 = 1528$ nm, respectively. In comparison, due to the well-separated work bands of INA and INB, when light waves at the two wavelengths are input from both INA and INB $(1\|1)$ (Figs. 5(e) and 5(f)), they do not interfere. Because the light waves at $\lambda_1 = 1490$ nm can not transmit through INB. Similarly, the light waves at $\lambda_2 = 1528$ nm have very low transmittance in INA. Here we notice that there is a small portion of light transmitting from one input to the other input (for example, from INA to INB at $\lambda_1 = 1490$ nm and from INB to INA at $\lambda_2 = 1528$ nm) at the junction of INA, INB, and OUT1 (shown in Figs. 5(c) and 5(d)). However, this effect does not influence the overall performance of the AOLG, as shown in Table 1.

Table 1. All-optical logic or gate truth table.

INA	INB	Logic output	Transmittance
0	0	0	0
1	0	1	0.86
0	1	1	0.90
1	1	1	0.82

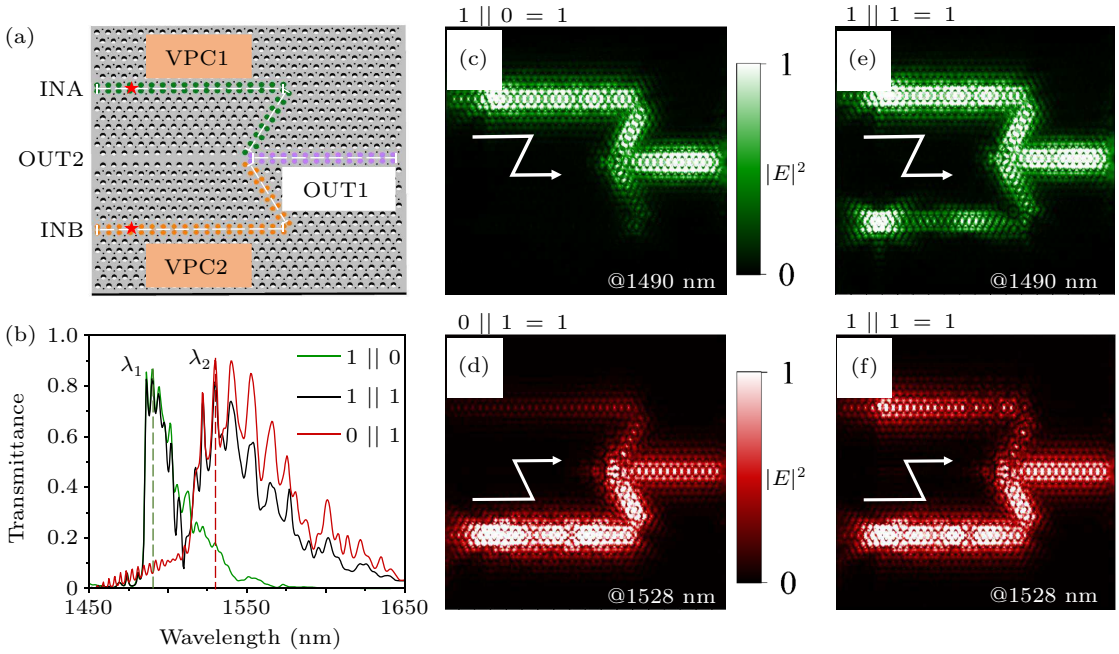


Fig. 5. The designed AOLG and its function. (a) 3D structural diagram of the ALOG gate. (b) Transmittance spectra of the AOLG in three different cases. Electric field intensity distributions at the wavelength of $\lambda_1 = 1490$ nm input from INA alone. (c) $(1\|0 = 1)$ and both INA and INB (e) $(1\|1 = 1)$, respectively. Electric field intensity distributions at the wavelength of $\lambda_2 = 1528$ nm input from INB alone. (d) $(0\|1 = 1)$ and both INA and INB. (f) $(1\|1 = 1)$, respectively.

The performance of the AOLG can be further studied by using the logic gate contrast function, which is defined as

$$R = 10\log\left(\frac{P_1}{P_0}\right), \tag{1}$$

where P_1 and P_0 are the transmittances of the output and the unexcited input, respectively. Most applications desire a high contrast ratio, which is challenging based on reported designs. The contrast ratio curves are shown in Figs. 6(a) and 6(b) for the inputs from INA and INB, respectively. The wavelength ranges are decided according to the working bands of INA and INB. The contrast ratios are 28.8 dB at $\lambda_1 = 1490$ nm in INA and 20.5 dB at $\lambda_2 = 1528$ nm in INB, which are much higher compared to state-of-the-art AOLGs.[34,36,37,40]

To show the advantages of using two well-separated working bands for the two inputs, we also perform the simulation on the logic gate composed of identical straight waveguides (details in supporting information S4). In this case, the transmittance in each case is relatively lower compared to the

separate design. That is due to the light transmitting from one input (INA or INB) to the other (INB or INA). Because both INA and INB can support the same edge states. The situation can be avoided by using different working bands for INA and INB, as demonstrated in this work. In this way, the forward transmittance of each input can be maximized, which is essential for any AOLGs for quantum computing since single photon transmission is necessary. Further, to demonstrate our design can work with different spin states (LCP or RCP light) due to the spin-valley locking effect, we perform the simulation on the input with different handedness (details in supporting information S5). Here LCP and RCP light is defined as logic "1" and "0", respectively. The output transmittance (TF $>$ 0.7) is still designated as logic "1". Due to the spin-valley locking effect, the LCP and RCP light propagates in opposite directions, resulting in high and low transmittances corresponding to the logic "1" and "0" states, respectively. In this way, the chirality of the logic gate allows using different spin states as different logic states, which is achieved among various AOLGs based on PC structures for the first time to the best of our knowledge.

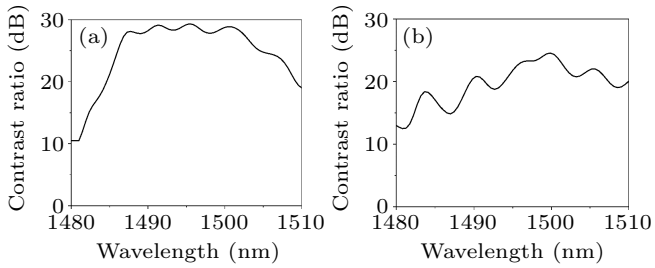


Fig. 6. Contrast ratio plots when light is only input from INA (a) and INB (b).

In order to demonstrate the unique defect immune transmission property of the our topological OR gate structures, we simulate the light transmission in the topological waveguides and the logic gates with defects, which could be introduced by fabrication errors. Here we simulated two types of defects: (i) Missing air holes in the waveguide (as shown in Fig. S7(a) in supporting information); (ii) Changing the radius of air holes (as shown in Fig. S7(b), 10% reduction in radius). The resulting transmittance spectra are shown in Fig. S7(c), in which only slight changes in the transmittance spectrum are observed, confirming the robustness of our design (details in supporting information S6). This property demonstrates high feasibility in the experimental realization of the designed structures.

5. Conclusion and perspectives

We have demonstrated a high-performance AOLG design based on a VPC structure. By tuning the working bands of the two inputs, we minimize the interference and cross-coupling between the inputs to ensure high transmittance output (up to 0.9) and high contrast ratio (up to 28.8 dB). Moreover, the chiral response of the logic gate due to the spin-valley locking effect allows using different spin states as inputs for quantum computing. The device's footprint is as small as 18 μm $\times$ 12 μm, which is suitable for high-density on-chip integration. In addition, the device is compatible with the CMOS nanofabrication technique. The design principle can be generally applied to design other photonic devices based on VPCs for broad applications.

Acknowledgments

Project supported by the National Key Research and Development Program of the Ministry of Science and Technology of China (Grant No. 2022YFA1404201), the National Natural Science Foundation of China (Grant No. 11904255), and the Key Research and Development Program of Shanxi Province (International Cooperation) (Grant No. 201903D421052).

References

[1] Panoiu N C, Bahl M and Osgood R M 2004 *Opt. Express.* **12** 1605
[2] Gomez V, Ramirez P, Cervera J, Ali M, Nasir S, Ensinger W and Mafe S 2018 *Electrochem. Commun.* **88** 52
[3] Zhu Y J, Huang X G and Mei X 2012 *Chin. Phys. Lett.* **29** 064214
[4] Zhang Y X, Liao Z Y, Pan J Q, Zhou F, Zhu H L, Zhao L J and Wang W 2009 *Chin. Phys. Lett.* **26** 104208
[5] Tu X, Chen Z M and Fu H Y 2019 *Acta Phys. Sin.* **68** 104210 (in Chinese)
[6] Zhang X, Li Z Q and Tong K 2014 *Acta Phys. Sin.* **63** 094207 (in Chinese)
[7] Han Z H, Jiang H, Tan Z Y, Cao J C and Cai Y J 2020 *Chin. Phys. B* **29** 084209
[8] Wang J H, Chen C M, Hu K W, Cheng R, Wang C X, Yi Y J, Sun X Q, Wang F, Li Z Y and Zhang D M 2019 *Chin. Phys. B* **28** 044207
[9] Chi F, Xu Q and Long X 2021 *Front. Phys.* **9** 819303
[10] Fu W, Xu M R, Liu X W, Zou C L, Zhong C C, Han X, Shen M H, Xu Y T, Cheng R S, Wang S H, Jiang L and Tang H 2021 *Phys. Rev. A.* **103** 053504
[11] Wang Y P, Wu C Q, Wang Z, Wang Y J, Yang S S and Sheng X Z 2009 *Chin. Phys. Lett.* **26** 074219
[12] Shehata M I and Mohammed N A 2016 *Opt. Quantum Electron.* **48** 336
[13] Ma S Z, Chen Z, Sun H Z and Dutta N K 2010 *Opt. Express* **18** 6417
[14] Kotb A, Zoiros K E and Li W 2021 *J. Supercomput.* **77** 14617
[15] Wang J, Sun J Q, Zhang X L, Huang D X and Fejer M M 2009 *IEEE J. Quantum Electron.* **45** 195
[16] Wang J, Sun J Q, Sun Q Z, Wang D L, Zhang X L, Huang D X and Fejer M M 2008 *IEEE. Photon. Technol. Lett.* **20** 211
[17] Xie Y Y, Yin Y Y, Song T T, Zhu Y C, Chai J X, Liu B C and Ye Y C 2022 *Optik* **255** 168684
[18] Law F K, Uddin M R, Chen A T C and Nakarmi B 2020 *Opt. Quantum. Electron.* **52** 314
[19] Zhang L, Ding J F, Tian Y H, Ji R Q, Yang L, Chen H T, Zhou P, Lu Y Y, Zhu W W and Min R 2012 *Opt. Express* **20** 11605
[20] Caballero L P, Povinelli M L, Ramirez J C, Guimaraes P S S and Neto O P V 2022 *Opt. Express* **30** 1976
[21] Sharma A, Goswami K, Mondal H, Datta T and Sen M 2022 *Opt. Quantum Electron.* **54** 90
[22] Hussein H M E, Ali T A and Rafat N H 2018 *Opt. Laser Technol.* **106** 385
[23] Fei H M, Zhang Q, Wu M, Lin H, Liu X, Yang Y B, Zhang M D, Guo R and Han X T 2020 *Appl. Opt.* **59** 4416

[24] Fei H M, Yan S, Wu M, Lin H, Yang Y B, Zhang M D and Han X T 2020 *Opt. Commun.* **477** 126346
[25] Fei H M, Wu M, Xu T, Lin H, Yang Y B, Liu X, Zhang M D and Cao B Z 2018 *J. Opt.* **20** 095004
[26] Fei H M, Wu M, Lin H, Liu X, Yang Y B, Zhang M D and Cao B Z 2019 *Superlatt. Microstruct.* **132** 106155
[27] Fei H M, Wu M, Lin H, Yang Y B, Liu X, Zhang M D and Cao B Z 2020 *Photon. Nanostruct.* **41** 100829
[28] Wu M, Fei H M, Lin H, Zhao X D, Yang Y B and Chen Z H 2021 *Acta Phys. Sin.* **70** 028501 (in Chinese)
[29] Zhi W Q, Fei H M, Han Y H, Wu M, Zhang M D, Liu X, Cao B Z and Yang Y B 2022 *Acta Phys. Sin.* **71** 038501 (in Chinese)
[30] Fei H M, Xu T, Liu X, Lin H, Chen Z H, Yang Y B, Zhang M D, Cao B Z and Liang J Q 2017 *Acta Phys. Sin.* **66** 204103 (in Chinese)
[31] Fei H M, Wu J J, Yang Y B, Liu X and Chen Z H 2015 *Photon. Nanostruct.* **17** 15
[32] Fei H M, Yan S, Xu Y C, Lin H, Wu M, Yang Y B, Chen Z H, Tian Y and Zhang Y M 2020 *Acta Phys. Sin.* **69** 184214 (in Chinese)
[33] Fan R R, Yang X L, Meng X F and Sun X W 2016 *J. Phys. D: Appl. Phys.* **49** 325104
[34] Jalali-Azizpoor M R, Soroosh M and Seifi-Kavian Y 2018 *Photon. Netw. Commun.* **36** 344
[35] Liu W, Yang D, Shen G, Tian H and Ji Y F 2013 *Opt. Laser Technol.* **50** 55
[36] Tang C R, Dou X, Lin Y, Yin H, Wu B and Zhao Q 2014 *Opt. Commun.* **316** 49
[37] Hussein H M E, Ali T A and Rafat N H 2018 *Opt. Commun.* **411** 175
[38] Rao D G S, Swarnakar S, Palacharla V, Raju K S R and Kumar S 2021 *Photon. Netw. Commun.* **41** 109
[39] Alipour-Banaei H, Serajmohammadi S and Mehdizadeh F 2017 *Optik* **130** 1214
[40] Ghadrdan M and Mansouri-Birjandi M A 2013 *Opt. Quantum Electron.* **45** 1027
[41] Chen X D, Shi F L, Liu H, Lu J C, Deng W M, Dai J Y, Cheng Q and Dong J W 2018 *Phys. Rev. Appl.* **10** 044002
[42] Prevedel R, Walther P, Tiefenbacher F, Bohl P, Kaltenbaek R, Jennewein T and Zeilinger A 2007 *Nature* **445** 65
[43] Chen Y, He X T, Cheng Y J, Qiu H Y, Feng L T, Zhang M, Dai D X, Guo G C, Dong J W and Ren X F 2021 *Phys. Rev. Lett.* **126** 230503
[44] Yang Y T, Xu Y F, Xu T, Wang H X, Jiang J H, Hu X and Hang Z H 2018 *Phys. Rev. Lett.* **120** 217401
[45] Skirlo S A, Lu L, Igarashi Y C, Yan Q H, Joannopoulos J and Soljacic M 2015 *Phys. Rev. Lett.* **115** 253901
[46] Gao F, Xue H R, Yang Z J, Lai K F, Yu Y, Lin X, Chong Y D, Shvets G and Zhang B L 2018 *Nat. Phys.* **14** 140
[47] Lu J C, Chen X D, Deng W M, Chen M and Dong J W 2018 *J. Opt.* **20** 075103
[48] Rechtsman M C, Zeuner J M, Plotnik Y, Lumer Y, Podolsky D, Dreisow F, Nolte S, Segev M and Szameit A 2013 *Nature* **496** 196
[49] Chao M H, Cheng B, Liu Q S, Zhang W J, Xu Y and Song G F 2021 *J. Opt.* **23** 115002
[50] He L, Zhang W X and Zhang X D 2019 *Opt. Express* **27** 25841
[51] Han Y H, Fei H M, Lin H, Zhang Y M, Zhang M D and Yang Y B 2021 *Opt. Commun.* **488** 126847
[52] Wu M, Yang Y B, Fei H M, Lin H, Han Y H, Zhao X D and Chen Z H 2022 *Opt. Express* **30** 6275
[53] Li H H 1980 *J. Phys. Chem. Ref. Data* **9** 561